Materials & Design 212 (2021) 110255

Contents lists available at ScienceDirect

Materials & Design

journal homepage: www.elsevier.com/locate/matdes

The study of hot deformation on laser cladding remanufactured 316L stainless steel

Yuehan Liu [a], Yaping Wang [a], Xin Xu [b], Christopher Hopper [a], Hongbiao Dong [c], Xingtao Wang [d], Hongbin Zhu [d,*], Jun Jiang [a,*]

[a] Department of Mechanical Engineering, Imperial College London, London SW7 2AZ, UK
[b] School of Materials, Sun Yat-Sen University (Shenzhen) and Southern Marine Science and Engineering Guangdong Laboratory (Zhuhai), 518107, China
[c] Department of Engineering, University of Leicester, Leicester LE1 7RH, UK
[d] CRRC Industrial Academy Co., Ltd, China

HIGHLIGHTS

- A hybrid method of laser cladding with subsequent hot compression technique is proposed to remanufacture/repair steel components.
- The hardness variation across cladding layer, welding interface and base metal can be removed utilizing the hot compression process.
- The mechanical properties of laser cladded 316L stainless steel increased after hot deformation.
- Analysis of microstructure evolution at cladding layer, welding interface and base metal part were performed.

GRAPHICAL ABSTRACT

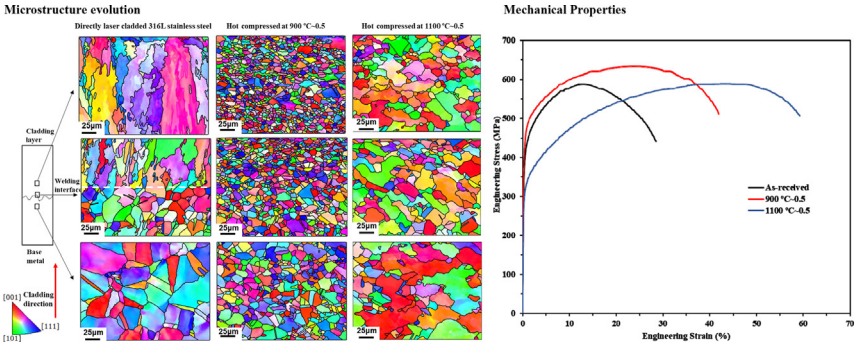

ARTICLE INFO

Article history:
Received 16 July 2021
Revised 27 October 2021
Accepted 15 November 2021
Available online 16 November 2021

Keywords:
Laser cladding remanufacturing
316L stainless steel
Hot deformation
Mechanical properties
Interfacial microstructure evolution

ABSTRACT

Laser cladding deposition (LCD) is widely used to remanufacture/repair workpieces because of its high design freedom to rebuild areas of damage. However, the process often introduces a columnar grain structure in the cladding layer, resulting in a large variation of microstructure and hardness across the cladding layer, welding interface, and base metal. Under fatigue and tensile loading, fractures can initiate in the lower hardness cladding layer. This study explores the feasibility of a new hybrid remanufacturing method integrating the LCD with a subsequent hot deformation process to refine grain structures, reduce hardness variations, and enhance mechanical properties. The effects of deformation temperatures and imposed plastic strains were studied by examining the microstructural and stress–strain behaviour of laser cladded 316L stainless steel. After LCD, compressive deformation was imposed at temperatures of 900 and 1100 °C, with engineering strain levels of 0.1 and 0.5. A high-quality metallurgical joint was achieved, with the optimal ultimate tensile strength and yield strength under process conditions of an engineering strain level of 0.5 imposed at 900 °C (35% improvement compared to the directly laser cladding remanufacturing process). Dynamic recrystallization process was observed by the electron back scatter diffraction technique to reveal the underlying mechanism.

1. Introduction

Steel components in service often endure thermal–mechanical stresses, local impact or fatigue damages leading to local defects

* Corresponding authors.
E-mail addresses: zhuhongbin@crrcgc.cc (H. Zhu), jun.jiang@imperial.ac.uk (J. Jiang).

https://doi.org/10.1016/j.matdes.2021.110255
0264-1275/Crown Copyright © 2021 Published by Elsevier Ltd.

and crack initiation [1]. These damaged components may be discarded as scraps or stored for later remanufacturing. To remanufacture/repair the used steel components, tungsten inert gas (TIG) welding has been widely employed [2,3]. However, as this is a fusion welding technique, it cannot be used to remanufacture the safety–critical steel components such as train axles to a high quality due to the high residual stress, weld interface distortion and large-size heat-affected zone (HAZ) [2]. Recently, researchers have found that additive manufacturing (AM) technology can be one of mainstream remanufacturing techniques in steels [4–8]. Compared to the TIG welding process, AM provides higher energy–density heat beams and smaller spot size of a heat source which contribute to a good metallurgical bonding quality, narrow melting interface and HAZ [4–9]. In addition, the large design freedom of AM enables the damaged area to be accurately located and remanufactured [1,2,10].

AM technology can be mainly categorized into powder bed fusion (PBF) and directed energy deposition (DED) [11]. PBF is a process where a component is built layer by layer using a laser to selectively fuse the surface layer of a bed of metallic powder. However, in the DED process, the powder metal feedstock is delivered directly to the required point, where it is then fused to the component surface [12]. This makes DED a preferred technique for remanufacturing large components. Laser cladding deposition (LCD), as one of the DED processes, has been widely applied for various industrial applications and is used in this study. Previous efforts have proved the feasibility of using laser cladding to remanufacture non-safety critical parts [13–15]. For example, Sun et al. characterized the microstructure of laser cladding repaired AISI 4340 steel and found coarse austenite and an acicular martensitic/bainite structure near the welding interface between the cladding layer and base metal [16]. The microstructure variations across the cladding layer, welding interface, and base metal resulted in a hardness gradient. It was noticed that a coarse grain size exhibited lower hardness. The same hardness gradient was found in the H13 hot-work tool steel components repaired by depositing H13 powder [2]. These hardness variations could lead to stress localization and are not acceptable in the remanufacture of safety- critical components.

The optimal strength, fracture toughness, and fatigue resistance for steel components should correlate with homogenous small grains [17]. However, coarse grains were found around the welding interface and these grew epitaxially through the AM cladding direction [18–22]. These epitaxial grains are due to the repeated melting and solidification dynamics during the cladding process and result in a columnar grain morphology [19]. The columnar grain structure could benefit thermal creep resistance due to the reduced grain boundary fraction [23]. However, it would have detrimental effects on the room temperature mechanical performance due to its low yield strength, fracture toughness, and fatigue life. Such lower yield strength is due to the Hall-Petch effect, where the strength of a material is shown to be inversely proportional to the square root of grain size [24,25]. Another contribution to the yield strength of materials is the dislocation density. According to the dislocation hardening theory, the strength is proportional to the square root of dislocation density [26]. Also, the stored dislocations act as an energy source to drive the recrystallization process. In previous studies, high dislocation content was found within the AMed grains [22]. Therefore, the dislocation density could be considered to improve the yield strength of AMed components. The internal thermal stress generates these stored dislocations introduced plasticity resulting from the rapid melting and solidifying process during deposition [27].

This study proposes to integrate a subsequent hot compression with the laser cladding remanufacture to address the above problems. This hot compression can refine the coarse-grained area, minimize the hardness gradient, and increase the fracture toughness. Previous research has examined the effect of hot forging (deformation) on AMed materials. Jiang et al. found a prominent enhancement of mechanical properties on AMed parts after hot forging [28]. The beneficial effects of high strain deformation on the 3D preform were later confirmed by Pruncu et al [29]. They found that the dynamic recrystallization (DRX) was induced during the hot deformation process and enhanced the mechanical properties. The applied deformation at elevated temperature also effectively closed the larger voids and pores in the parts. This concluded that the hot compression process was beneficial in refining the grain size and reducing the void content. However, no research was found studying the effects of hot deformation on the base/AM interface of laser cladding remanufactured components. In this study, the influence of hot plastic deformation on laser cladding remanufacturing will be addressed, particularly the evolution of grain morphology and size at the cladding layer/welding interface. The mechanisms involved in creating enhanced mechanical properties will be examined through grain microstructure characterizations.

316L stainless steel (316L SS) was selected as the demonstration material in this study because of its wide use in nuclear, maritime, power generation, oil, and aerospace applications thanks to its high corrosion resistance and strength [30]. It has been widely applied in AM [31–33]. The grain microstructure of AMed 316L SS is easy to be characterized because it is a single-phase austenite steel [34]. The work of using DED to repair AMed 316L SS was conducted and distinct microstructure variation along repaired layer and damaged part was characterized [5]. Clear insight into the grain deformation and microstructure evolution along the cladding layer, welding interface and base metal during the hot deformation process will be gained for 316L SS in this study.

This work aims to study the effects of hot deformation on the tensile properties, hardness, and microstructure across the laser cladding remanufactured 316L SS interface. Four thermal–mechanical conditions were applied, using engineering strain levels of 0.1 and 0.5 at temperatures of 900 °C and 1100 °C. The strain rate applied was 0.01 s^{-1}. These hot deformation parameters are appropriate for the industrial hot forging conditions [29,35] and can trigger the DRX in 316L SS. Detailed tensile stress–strain behaviour and microhardness values were obtained. Electron backscatter diffraction (EBSD) characterization was conducted across the cladding layer, welding interface, and the base metal. The microstructure evolution as functions of strain and temperature was shown. The obtained EBSD crystal orientation information, detailed grain morphology, grain size, and geometrically necessary dislocation (GND) density analyses were carried out to relate the hot deformation effects to the observed corresponding mechanical properties.

2. Methodology

2.1. Materials and specimen preparation

The materials used for LCD remanufacturing were cold worked single-phase 316L SS for the component and gas-atomized 316L SS powder as the cladding material. The typical composition of 316L SS is listed in Table 1. Before the laser cladding process, the base metal surface was mechanically ground. The 316L SS powder was deposited on the base metal using a RC-LDM8060 Laser Deposition machine (Sailong Metal Materials Co., Ltd., China). The process is illustrated in Fig. 1.

An inert gas was used to deliver the metal powder with a constant flow rate as shown in Fig. 1(a). The laser cladding process parameters are listed in Table 2. To mimic the remanufacturing process and test the interface's strength, the powder was vertically

Table 1
Chemical composition of AM 316L stainless steel powder.

Elements	Fe	Cr	Ni	Mo	Mn	Si	N	O	P	C
Mass (%)	Balance	17.42	12.64	2.10	1.16	0.58	0.036	0.0066	0.016	0.021

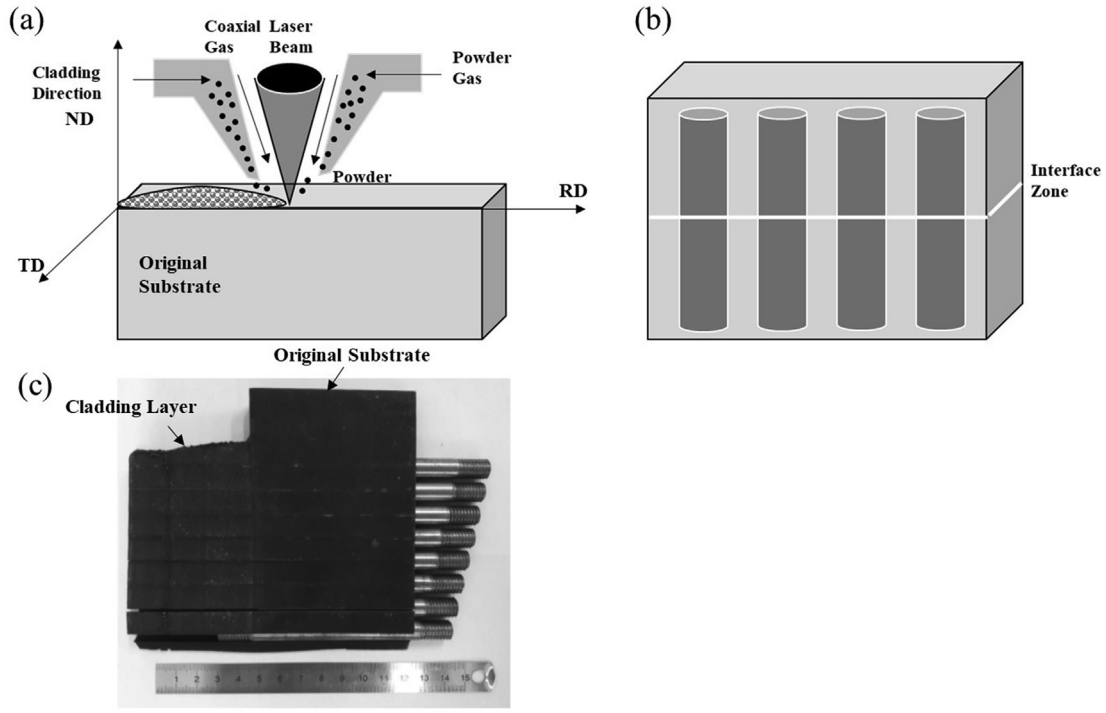

Fig. 1. (a) Schematic diagram to illustrate the LCD process, cladding direction, and (b)(c) present the EDM direction to machine samples with half laser clad 316L SS and half base 316L SS substrate.

Table 2
Laser cladding process variables

Laser Power (W)	Beam Traverse Speed (mm/min)	Hatching Pitch (mm)	Layer Thickness (mm)	Gas Flow Rate (L/min)
1000	800	0.3	1	5

deposited on the base metal layer by layer to the same height as the base part itself. The LCD remanufactured specimens consist of half-substrate original 316L SS and half-AMed material, such that the interface between the base and AM part was at the middle of the block. After the laser cladding, cylindrical specimens of 10 mm diameter were machined out by the electro-discharge machining (EDM) with their principal axis and cladding direction parallel to each other, as illustrated in Fig. 1(b) and (c).

2.2. Hot compression process

The as-received specimens were hot compressed using a Gleeble 3800 thermo-mechanical simulator, as schematically shown in Fig. 2(a). To measure and control the temperature at the AM-base metal interface, a pair of thermocouples were welded to the centre of the specimen. The detailed thermal history profile during the hot compression process is given in Fig. 2(b). The specimens were firstly heated at a rate of 10 °C/s to a temperature 25 °C below the designed hot compression temperature and then slowly heated to the designed temperature at a rate of 2 °C/s. Subsequently, they were soaked at the hot compression temperature for 3 min to unify the temperature distribution. The two temperature parameters applied in this study were 900 °C and 1100 °C respectively. The specimens were then compressed at a constant strain rate 0.01 s^{-1} to the engineering strain levels of 0.1 and 0.5 as measured by the stroke displacement. The specimens were then air cooled to room temperature. It is noted that four hot deformation conditions were applied: 900 °C ∼ 0.1, 900 °C ∼ 0.5, 1100 °C ∼ 0.1, and 1100 °C ∼ 0.5 respectively. For each condition, three samples were produced. One of these three specimens was used for EBSD characterization and microhardness test. The other specimens were used to perform the tensile test to check the repeatability of the results. The flow stress–strain curves during the hot compression process are shown in Fig. 2(c) that were collected and calculated from the Gleeble data library.

2.3. Microstructure characterization

EBSD characterization was conducted on the hot compressed specimens to reveal the grain and GND density distribution. One set of four specimens was cut along longitudinal cross-section as shown in Fig. 2(d) and ground progressively using SiC grinding papers from 600 to 4000 grit. Then they were polished by oxide polishing suspension (OPS) for 15 min to a mirror surface finish. A Hitachi 3400 scanning electron microscope (SEM) equipped with an e-FlashHR EBSD detector (Bruker) was used to characterize the

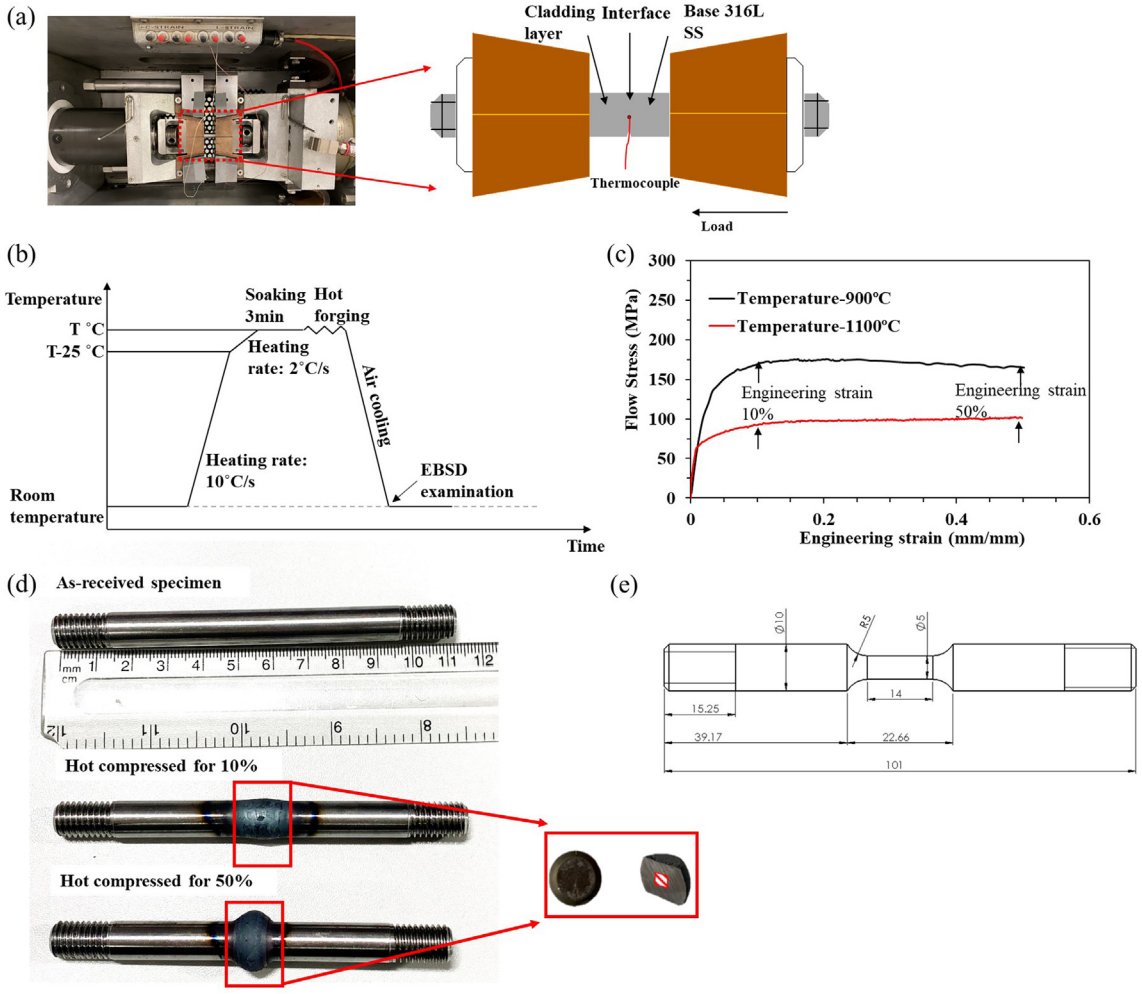

Fig. 2. (a) Gleeble 3800 hot compression experiment setup; (b) Heat schematic of hot compression process; (c) Flow stress curves during the hot compression process and four compression conditions were undertook as marked; (d) As-received specimen geometry and specimens after hot compression (The marked parts were cut for microstructure characterization); (e) The geometry of tensile test specimens machined from the hot compressed blanks.

RD (rolling direction)-ND (normal direction) plane microstructure. 248 μm × 187 μm EBSD mappings were acquired at 1 μm step size and 500x magnification. The grain size and GND density were estimated by using Quantax Esprit software and MTEX toolbox, and the misorientation used to define grain boundaries was set at 5°. It is noted that the specimens were scanned at the interface and 2 mm away from the interface where is within the isothermal range such that the microstructure of the cladding layer, interface area, and base metal were all included in mappings.

The grain size was calculated after removing grains below 5 pixels in size. The average grain size is calculated by using an area-weighted averaging approach, which is given by,

$$\bar{d} = \frac{1}{\sum_{i=0}^{n} A_i} \sum_{i=0}^{n} A_i d_i$$

where n is the number of grains on the map, A_i is the area of grain i and d_i is the diameter of grain i.

The GND density in this study was estimated by the embedded function in the MTEX toolbox. Briefly, EBSD can give the local orientation of neighbouring points in a grid on a planar surface. The lattice curvature tensors were computed by taking the directional derivative of the rotation tensor defined for every pixel in the horizontal-vertical directions [36]. Six lattice curvature tensors were used to determine five components of the dislocation density tensor and one difference between two other components. The GND content can be subsequently estimated by an energy-based linear optimization method [36]. More details about the GND estimation mathematical framework can be found in Pantleon's work [36]. Optical microscope (OM) was also applied for the microstructural characterisation. The polished samples were immersed into 1 g/mL oxalic acid for 40 s with a voltage 8 V to reveal its microstructure under the OM.

2.4. Tensile and microhardness tests

Fig. 2(d) & (e) show the dimension of the tensile test specimen machined out from the hot compressed samples. Note that no standard tensile sample geometry was machined because only the middle part was hot compressed. The as-received specimen without hot compression was also machined to the same geometry as a benchmark. All the specimens were machined longitudinally, and the loading axis was oriented along the cladding direction, such that the welding interface was subjected to normal tensile stress. The tensile test was conducted at room temperature on an Instron testing machine with a 50 kN load cell, using an extension rate of 0.3 mm/min. An extensometer measured the strain. For each hot compression condition, the tensile tests were repeated twice to confirm repeatability.

The microhardness test was conducted on the polished specimen surface under 300 N (HV30) load at room temperature with 10 s dwell time using a Zwick hardness tester. To map the microhardness across the interface areas, 11 hardness measuring points at a spacing of 1 mm were conducted across the base metal, interface and cladding layer, for which the middle point is at the interface. For each point, to ensure the precision, five hardness measurements along the radial direction were made to take the mean value and remove the outliers.

3. Experimental results

3.1. Initial microstructure of laser cladding remanufactured specimens

Fig. 3 shows the EBSD maps and inverse pole figure (IPF) maps of as-received laser clad 316L SS at cladding layer, interface, and base metal. Overall, the microstructure distributions across these three distinct regions are highly heterogeneous in terms of grain size, orientation, and morphology. Fig. 3(a) shows an epitaxial columnar grain morphology in the cladding layer. This feature was expected to be common in AM parts due to the continuous melting and solidification dynamics [19]. The previously deposited layers were re-melted such that grain nucleation before solidification was prevented. In addition, a large thermal gradient was induced by the molten pool [19]. Since the heat flux was unidirectional from the molten pool to the previously solidified region, grains grew along the cladding direction [5]. For this study, high laser power and slow deposition speed were applied to prevent void formation, leading to obvious coarse grains at the cladding layer [37]. Fig. 3(g) presents a strong texture along the radial direction in the (100) pole figure. The distinctive crystallographic texture could contribute to the anisotropic properties in the clad part [38,39]. Fig. 3(b) exhibits a clear continuous welding zone consisting of a fusion zone and an un-melted base metal zone, which is comparable with previous joining work done by Hinojos et al. [8].

The fusion zone exhibits a narrow zone of large grains, as shown in Fig. 3(b) above the dashed line indicating the weld line. Below the dashed line in the un-melted zone, a finer grains distribution is shown in Fig. 3(b). These finer grains (~10 μm grain size) with high angle grain boundaries (HAGBs) could be generated by static recrystallization during the cladding process which depends on the cold working history of the damaged 316L SS base metal and cladding duration. The high orientation gradient (fading colour within grains) is shown in the matrix material as seen in Fig. 3(c) and the low angle grain boundaries (LAGBs) distribution in Fig. 3(f) indicates the highly stored plastic strain energy (i.e. high dislocation content) which could generate nucleation sites for recrystallization. In addition, the grains in the cladding layer, Fig. 3(a), are obviously larger than the grains at the welding interface. This could be due to the difference in the cooling rates. The amount of heat transferred through the conduction is reduced when depositing away from the cold substrate, resulting in a lower cooling rate as the cladding layer is built up. Therefore, the melt pool size and grain size vary along with the cladding height [40]. Fig. 3(d) also shows several LAGBs (i.e. subgrain boundaries) inside of grains in the cladding layer which indicates highly stored dislocations produced by thermal stress.

3.2. The specimen microstructure after hot compression processing

Following the hot compression processing, sections were taken from the specimens and subject to EBSD, scanning electron microscope (SEM) and optical microscopy (OM) analysis. Fig. 4(a)-(l)

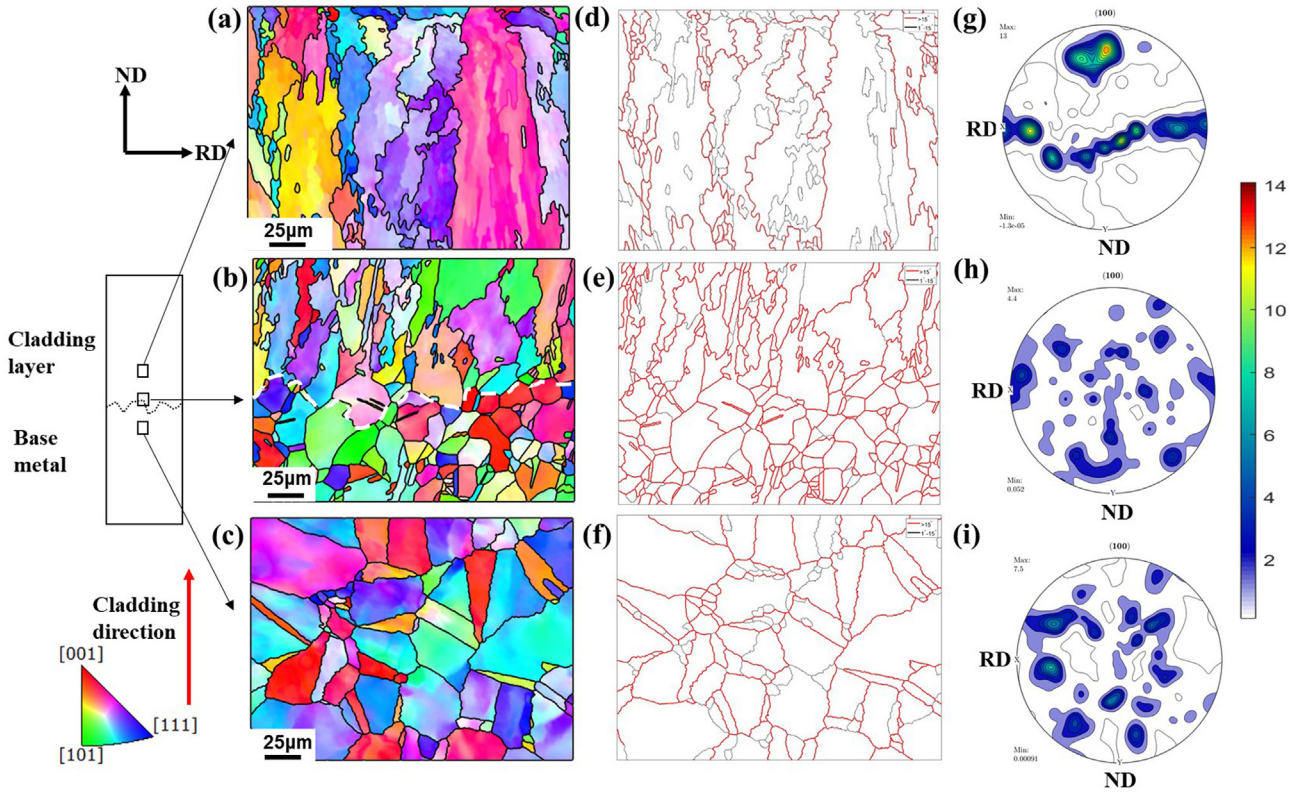

Fig. 3. The EBSD IPF showing the microstructure of as-received specimen on different areas (a) cladding layer (b) interface (c) base metal, (d), (e) and (f) are corresponding grain boundary misorientation distribution figures, (g), (h), (i) are corresponding (100) pole figures. The rolling direction (RD) is horizontal, and the cladding direction is along the normal direction (ND) that is vertical.

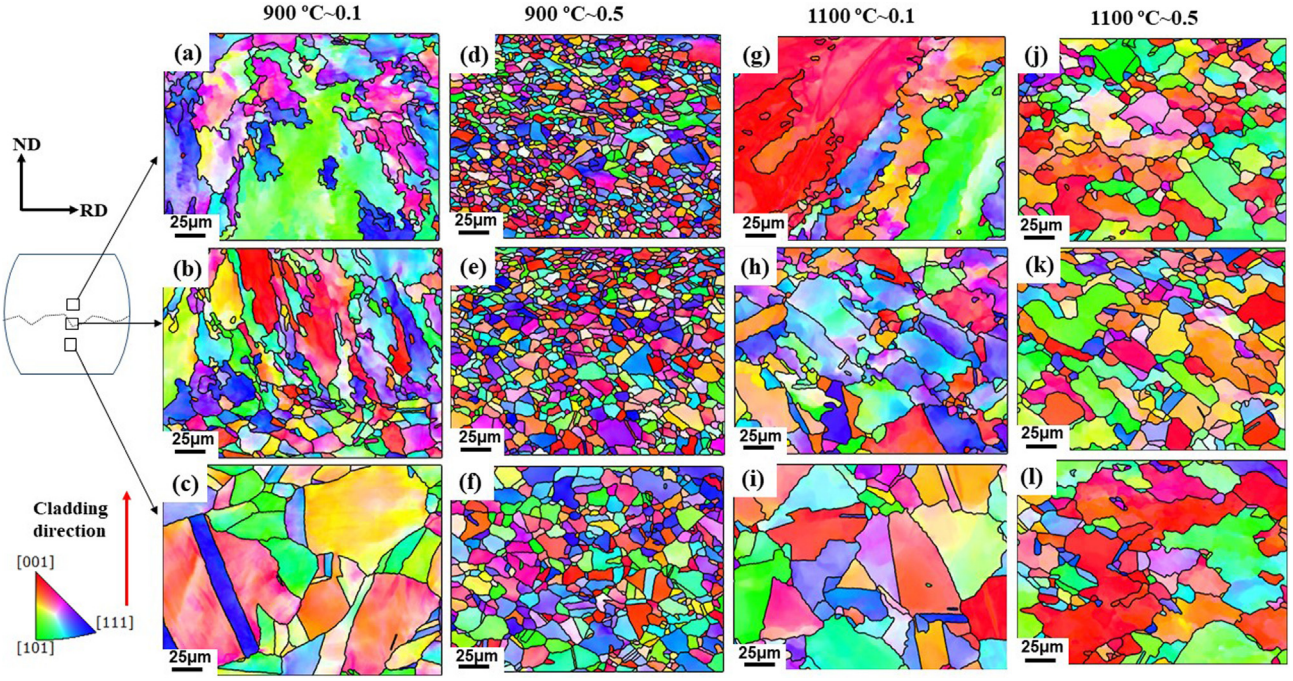

Fig. 4. The overview of EBSD IPF maps of laser cladding specimens after four hot compression conditions. Three areas were characterized. Note that (a), (d), (g) and (j) are cladding areas; (b), (e), (h) and (k) are bonding areas; (c), (f), (i) and (l) are base metal areas.

shows the EBSD IPF maps of hot compressed specimens at 900 °C ∼ 0.1 plastic strain, 900 °C ∼ 0.5 plastic strain, 1100 °C ∼ 0.1 plastic strain, and 1100 °C ∼ 0.5 plastic strain respectively. The microstructures at −2, 0, and 2 mm from the interface between the cladding and base metals are shown.

It is found that at a strain level of 0.5, the grain sizes at the cladding layer, interface and base metal are almost identical. The grain size did, however, increase as the compression temperature increased. These demonstrated the competing processes of grain growth and grain refinement occurring during the DRX. A homogeneous grain distribution with a considerably smaller grain size is observed at specimen compressed at the condition of 900 °C ∼ 0.5. This microstructure would suggest potentially better mechanical properties compared with the other three specimens. Compared with the initial as-received specimen, the hot compression at 900 °C ∼ 0.1 has little influence on the microstructure. For the specimen compressed at 1100 °C ∼ 0.1, DRX is seen at the coarse-grained welding interface, as indicated by the necklace structures found around the grain boundaries. However, the grains in the cladding layer are elongated along the cladding direction, as shown in Fig. 4(g). When compressed to the engineering strain level of 0.5 at 1100 °C, the relatively coarse grains distribute evenly across the cladding layer, interface, and the base metal.

Fig. 5 shows the SEM and OM graphs under different magnifications at the bonding interface. The grains grow along the cladding direction which conform with the EBSD results. Vimineous cellular structures are observed at welding line of as-received specimen and specimens compressed to ∼ 0.1 strain level. For specimens compressed to ∼ 0.5, obvious deformation of molten pool is shown in Fig. 5(g) and (m). The cladding layer exhibits obvious different grain morphology other than cellular structure which is shown in the red ovals.

Fig. 6 shows the quantitative analysis of the average grain size of specimens compressed at various conditions. For the specimen compressed at 900 °C ∼ 0.5, average grain size decreases to approximately 9, 11 and 16 μm at cladding layer, interface, and base metal respectively, due to the DRX influence. After hot compression at 900 °C ∼ 0.1, however, the average grain size across the cladding layer exhibits same grain size variation as the original as-received specimen which is influenced by small, necklaced grains around the grain boundary. Larger grains are shown in both cladding layer and base metal and the grain size of base metal increases from 42 μm to 68 μm. However, comparing the specimen deformed at 1100 °C ∼ 0.1 with the as-received one, the grain size of cladding layer increases from 78 μm to 92 μm, the grain size at interface increases from 30 μm to 36 μm and the grain size of base metal increases from 42 μm to 58 μm. For the specimen compressed at 1100 °C ∼ 0.5, the grains become roughly homogenous along the cladding layer and interface that are approximately 30 μm. But the grains at the base metal also increase slightly.

Fig. 7 shows the recrystallized volume fraction of the three distinct regions for the specimen under the designed hot deformation conditions. Note that in the DRX process and the formation of new grains, dislocation generation, dislocation storage, and grain growth are also occurring simultaneously. The commonly used grain orientation spread (GOS) method in the static recrystallization process, checking the misorientation angle spread within each grain, which is no longer appropriate in DRX because the continuous plastic deformation generates new dislocations stored within those newly formed grains [41]. In this case, as the initial grain size is large and most of the recrystallized grains are relatively small, it was assumed that the grains with sizes below that the average value of un-deformed grain were defined as recrystallised grains.

The specimen deformed at 900 °C to 0.5 strain appears to have fully recrystallized, as shown in Fig. 7(g)-(i). For the specimen deformed at 900 °C ∼ 0.1, most grains are in similar size as the grains in the as-received sample, and only partial smaller grains were nucleated at the grain boundary. Hence the grains mainly grew without much refinement in this stage. For the specimen deformed at 1100 °C ∼ 0.1, small grains are observed that indicated the grains started to nucleate. Grain growth was found at 1100 °C ∼ 0.5. Compared with the specimen deformed at

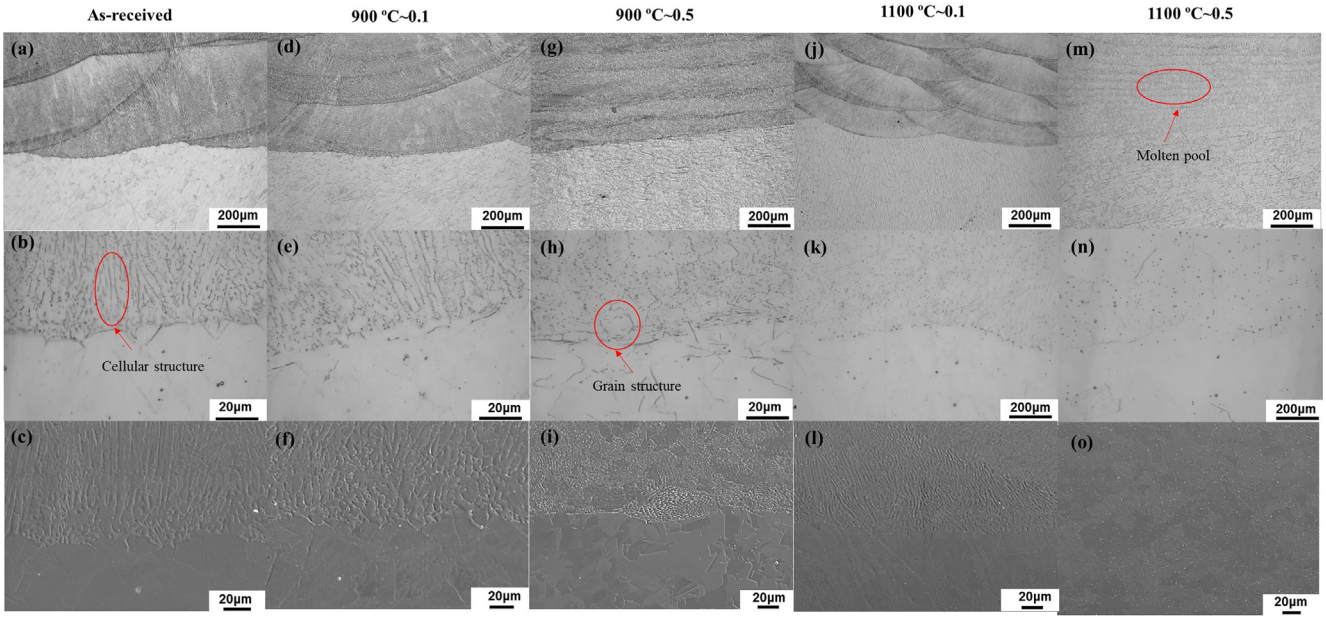

Fig. 5. The microstructure of bonding interface under different magnification. Note that (a), (b) and (c) are interfaces for as-received specimens; (d), (e) and (f) are interfaces compressed at 900 °C ~ engineering strain 0.1; (g), (h) and (i) are interfaces compressed at 900 °C ~ engineering strain 0.5; (j), (k) and (l) are interfaces compressed at 1100 °C ~ engineering strain 0.1; (m), (n) and (o) are interfaces compressed at 1100 °C ~ engineering strain 0.5.

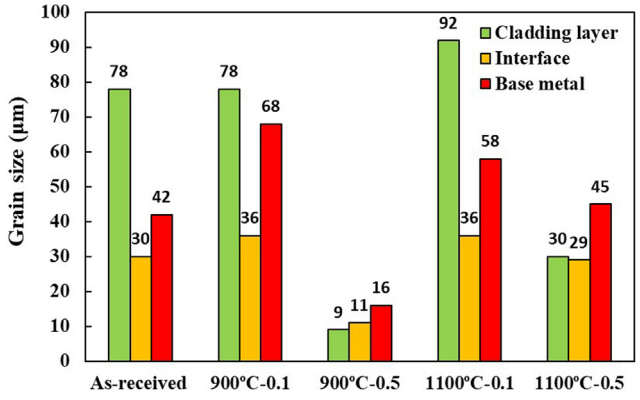

Fig. 6. The average grain size of laser cladding 316L SS at initial, compressed at 900 °C ~ engineering strain 0.1; 900 °C ~ engineering strain 0.5; 1100 °C ~ engineering strain 0.1; 1100 °C ~ engineering strain 0.5.

900 °C ~ 0.5, it is hard to distinguish whether grains were recrystallized before they grew. This is due to limitations of the estimation method employed. The higher strain level and lower deformation temperature are shown to promote a more uniform fine grain microstructure.

Fig. 8 shows the LAGBs and HAGBs distribution of different regions for specimens compressed under different conditions. For specimen compressed at 900 °C ~ 0.1, Fig. 8(d) shows a number of LAGBs which indicates dislocation introduction at small strain level where the driving force is insufficient for DRX occurrence. For the specimen compressed at 900 °C ~ 0.5, most grains were treated as recrystallized grains in Fig. 7(g)-(i). This observation confirms with the HAGBs results seen in Fig. 8(g)-(i). For the specimen compressed at 1100 °C, as the nature of the DRX process, dislocations were continuously generated and rearranged to form LAGBs. However, these grains with LAGBs cannot account as non-recrystallized grains. Therefore, these LAGBs and HAGBs maps only give a limited insight to the recrystallization process.

3.3. GND density distribution

The stored dislocation density within a material will strengthen that material [42], as well as storing plastic strain energy for new grain nucleation [43]. Hence it is important to understand the evolution of dislocation density as a function of strain and temperature to explain the corresponding mechanical properties. A group of dislocations can be defined as geometrically necessary dislocations (GNDs) or statistically stored dislocations (SSDs) depending on their contribution to the geometrical curvature changes in the probed lattice [44]. GNDs caused by a strain gradient result in a lattice curvature manifested as the grain misorientation [45]. Whereas the SSDs are dislocations that do not result in lattice curvature. This definition is ambiguous as a dislocation can be GND or SSD depending on the probing step size. In practice, only a fraction of total dislocation density can be estimated based on its misorientation measurement due to the limited spatial resolution and acquisition time. However, these GNDs density maps do provide an excellent statistical indication of overall dislocation density distribution, especially at elevated temperature conditions, in which the dislocation climb and cross-slip are considerably promoted by the thermal energy to annihilate the randomly distributed SSDs and form the energetically favourable GNDs. These have been confirmed by other dislocation characterization methods such as transmission Kikuchi diffraction (TKD) [46].

Fig. 9(a)-(c) present the GNDs density maps of the as-received specimen at cladding layer, interface, and base area respectively. In general, a high dislocation content is found along the cladding direction. This attributes to thermally induced plasticity, which is consistent with the results in the literature [22,47]. In the interface region, no obvious "red" spot could be found. At the base metal region, the GNDs appear accumulated along the grain boundaries rather than in the interior of the grains, indicating that the base metal is not in a completely annealed state.

After the thermo-mechanical deformation, the GNDs density distribution changes significantly as shown in Fig. 10. For the specimen compressed at the condition of 900 °C ~ 0.1, the imposed plastic deformation considerably increased the stored GNDs den-

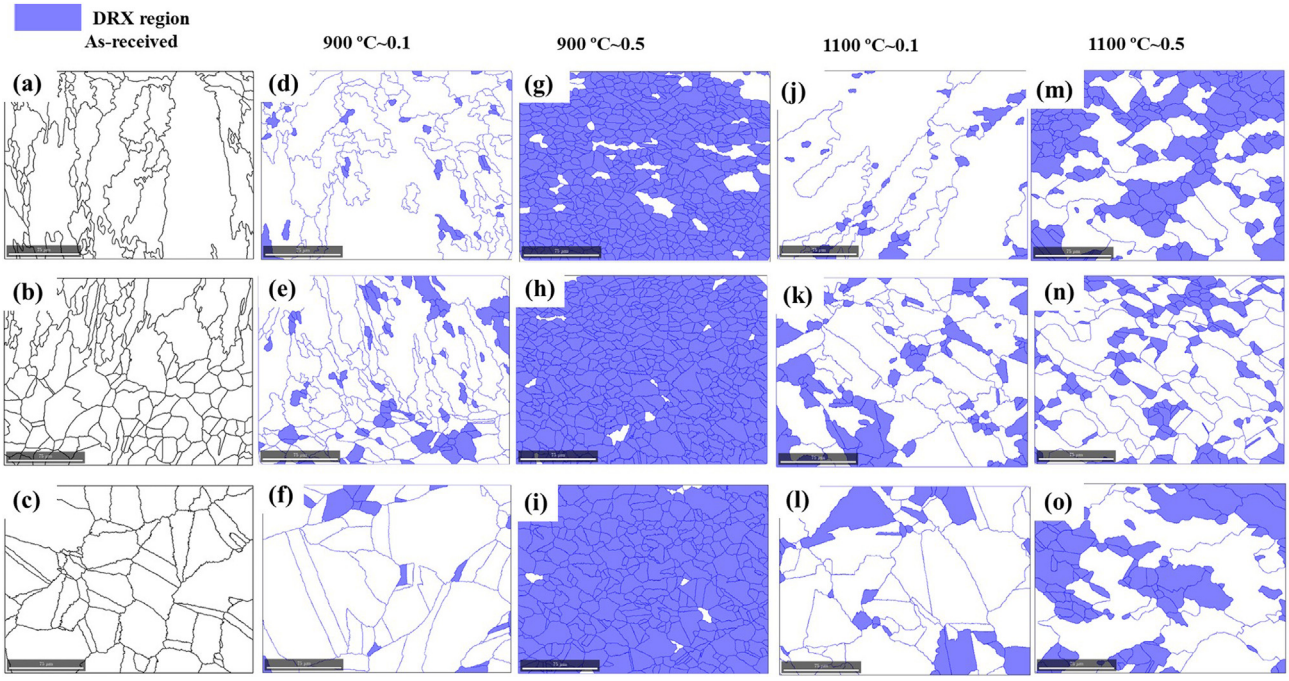

Fig. 7. Recrystallized grains of 316L SS at different compression conditions 900 °C ∼ engineering strain 0.1; 900 °C ∼ engineering strain 0.5; 1100 °C ∼ engineering strain 0.1; 1100 °C ∼ engineering strain 0.5. (a), (d), (g), (j) and (m) present cladding area; (b), (e), (h), (k) and (n) present bonding zone; (c), (f), (i), (l) and (o) present base metal part.

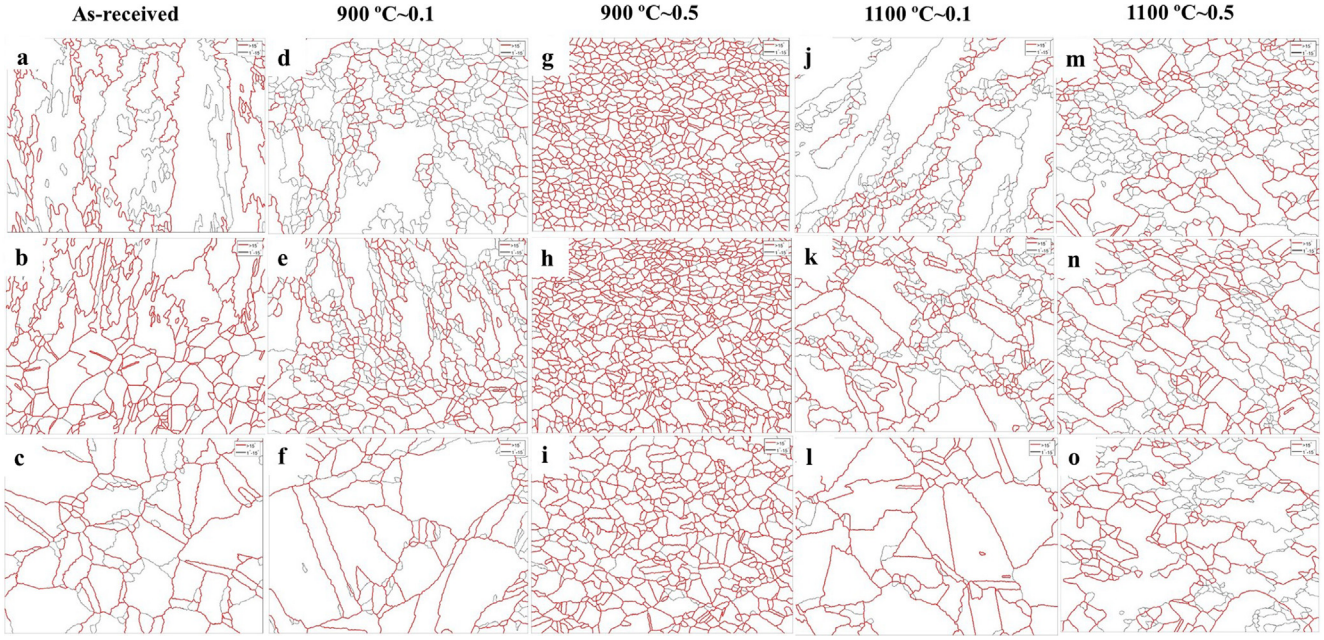

Fig. 8. Distribution of HAGBs (red lines) and LAGBs (black lines) of laser cladding specimens after four hot compression conditions. Note that (a), (d), (g), (j) and (m) are cladding areas; (b), (e), (h), (k) and (n) are bonding areas; (c), (f), (i), (l) and (o) are base metal areas. (For interpretation of the references to colour in this figure legend, the reader is referred to the web version of this article.)

sity. However, this stored GNDs density was insufficient to trigger the recrystallization. Instead, the grain growth was found to occur. This agrees with the observed low recrystallized volume fraction, as shown in Fig. 7(d)-(f).

For the specimen compressed at 900 °C to an engineering strain level of 0.5, obvious recrystallization occurred. The new grains consumed the previously heavily deformed grains and thus lowered the overall GNDs density. There is a higher GNDs density in the cladding area than the base material. It could imply that the DRX occurred earlier in the base metal region since more GNDs were consumed there.

The GND density distribution was generally lower but more uniform across the three distinct regions in the specimen compressed at 1100 °C rather than the 900 °C. This might suggest that the dislocation annihilation processes were very active at a higher temperature. Another possible reason is concerned that the grain boundary migration consumed many dislocations. However, the concurrence of dynamic recovery (DRV), dislocation generation

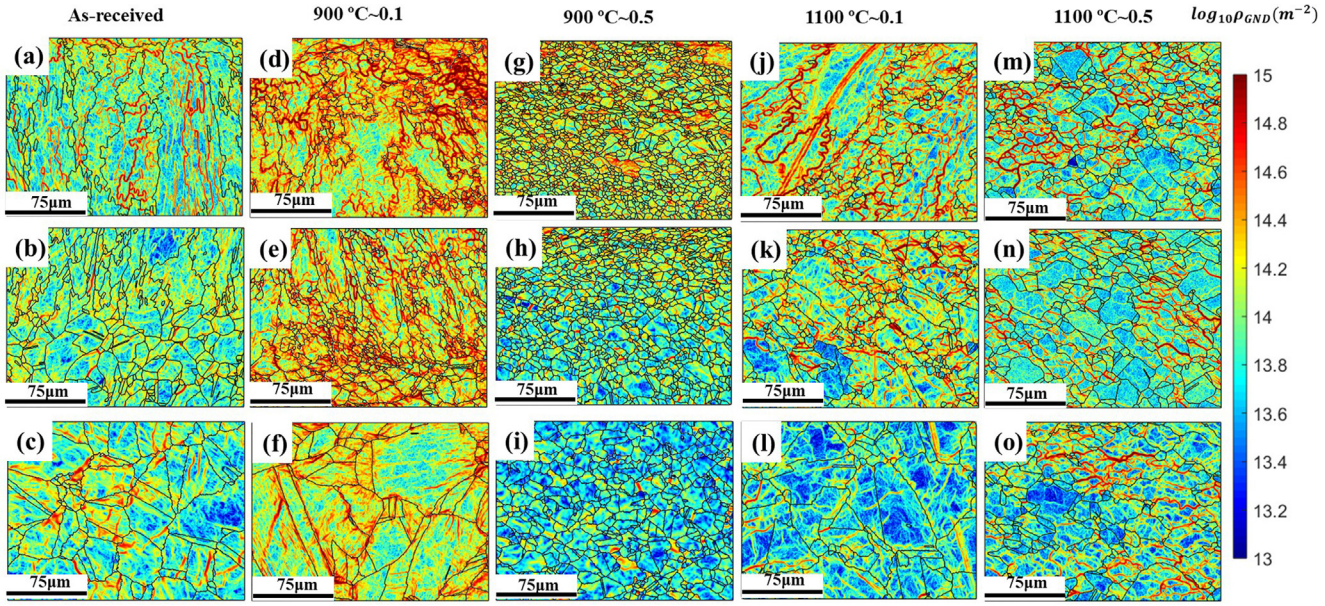

Fig. 9. GND density maps of laser cladding specimens of the as-received and ones being hot compressed at the four conditions. Three areas were characterized. Note that (a), (d), (g), (j) and (m) are cladding area. (b), (e), (h), (k) and (n) are bonding area. (c), (f), (i), (l) and (o) are base metal area. The colour scale is at the log10 and the black lines correspond to the grain boundaries.

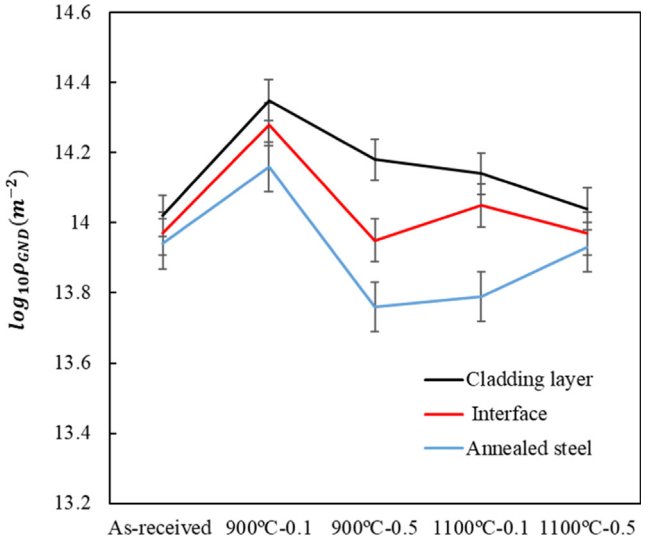

Fig. 10. The statistical analysis of GND density distribution of all five samples as shown in the x-axis. Note that the black line indicates the cladding layer, the red line indicates the interface area and the blue line indicates the base metal. The geometrical mean and standard division for each map is calculated and plotted as the error bars. (For interpretation of the references to colour in this figure legend, the reader is referred to the web version of this article.)

and DRX in the hot deformation process made it difficult to distinguish them quantitively.

3.4. Tensile stress–strain behaviour

Fig. 11 shows the tensile stress–strain curve of the as-received laser clad remanufactured specimen and the other four hot compressed specimens. The as-received specimens fractured at laser clad part that close to the middle interface during the tensile test. This fracture region is the coarse-grained fusion zone, which is quite typical for laser cladding specimens. In addition, the measured tensile properties were compared with the traditional cast and wrought 316L SS materials, as shown in Table 3. The hot compressed specimens exhibits considerably higher ultimate tensile strength (UTS), or higher ductility compared with the as-received specimen. The results prove that the subsequent hot compression enhances the mechanical properties of the laser cladding remanufactured components.

Compared with the as-received specimen, the specimen compressed at 900 °C to an engineering strain level of 0.5 gives the best tensile properties for yield strength and UTS. The maximum UTS raises to 633 MPa with an elongation of 41%. The ductility is ~ 50% higher than the as-received specimen. However, for the specimen deformed at the same temperature of 900 °C but a lower strain level of 0.1, though the UTS is almost the same as the as-received specimen, the ductility only improves mildly from 28% to 33%. For the specimens compressed at the higher temperature (1100 °C) to strain levels of 0.1 and 0.5, similar levels of UTS are achieved, but the ductility improved from 28% to 58% compared with the as-received specimen. However, the yield strength (~260 MPa) for these hot compressed samples drop significantly, which is much lower than the as-received (~338 MPa) or the lower temperature compressed ones (~456 MPa).

3.5. Microhardness test

The microhardness test was conducted along the cladding direction of specimens. As shown in Fig. 12, an abrupt hardness variation across the interface is observed in the as-received specimen. Such hardness variation was eliminated through the subsequent hot deformation process.

The hardness decreases from 175 HV to 165 HV along the cladding direction for the initial as-received specimen. This is consistent with the results from Chechik et al. [40]. This might attribute to the decreases in cooling rate with increasing cladding height. The hardness increases to 230 HV at the interface and then decreases gradually to ~ 215 HV in the base metal region.

After the hot deformation, the hardness distribution is approximately uniform. For the specimen compressed at 900 °C, the hardness of the cladding layer is higher than that in its base metal. The hardness at the cladding layer ranges from ~ 190 HV to ~ 200 HV, and the hardness at base metal is around 188 HV. The hardness of

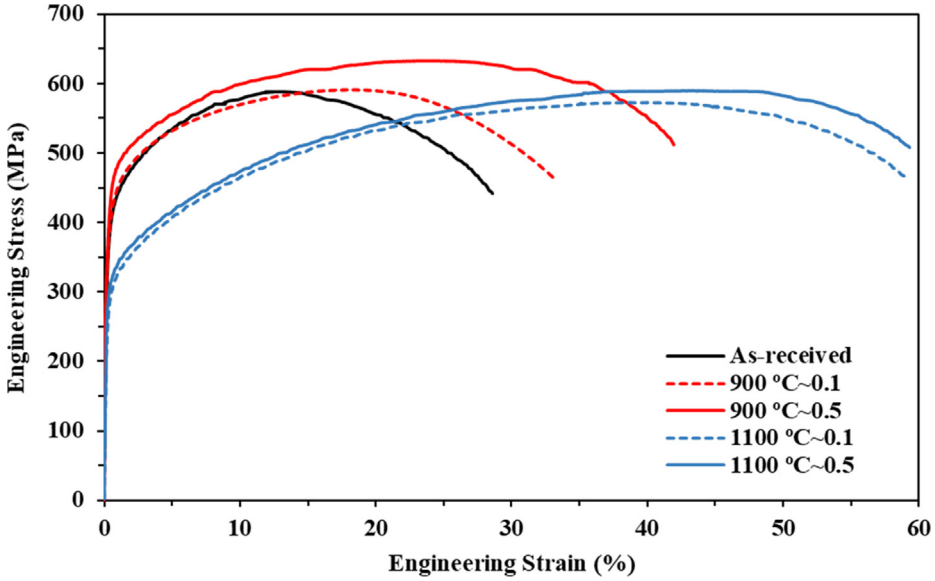

Fig. 11. Engineering stress–strain curve of as-received laser clad 316L SS and subsequently hot compressed ones.

Table 3
Tensile properties of the cast and wrought 316L SS specimens in the literature, the as-received and subsequently hot compressed 316L SS specimens in this study.

Conditions	Yield Strength (MPa)	Ultimate Tensile Strength (MPa)	Elongation (%)	Ref
Cast	262	553	55	[48]
Wrought (cold finished)	255–310	525–623	30	[48]
As-received	338	586–588	28–29	
As-received + hot deformed at 900C ~ 0.1	378	589–591	31–33	
As-received + hot deformed at 900C ~ 0.5	456	624–633	41–47	
As-received + hot deformed at 1100C ~ 0.1	241	572–575	55–58	
As-received + hot deformed at 1100C ~ 0.5	260	589–596	56–58	

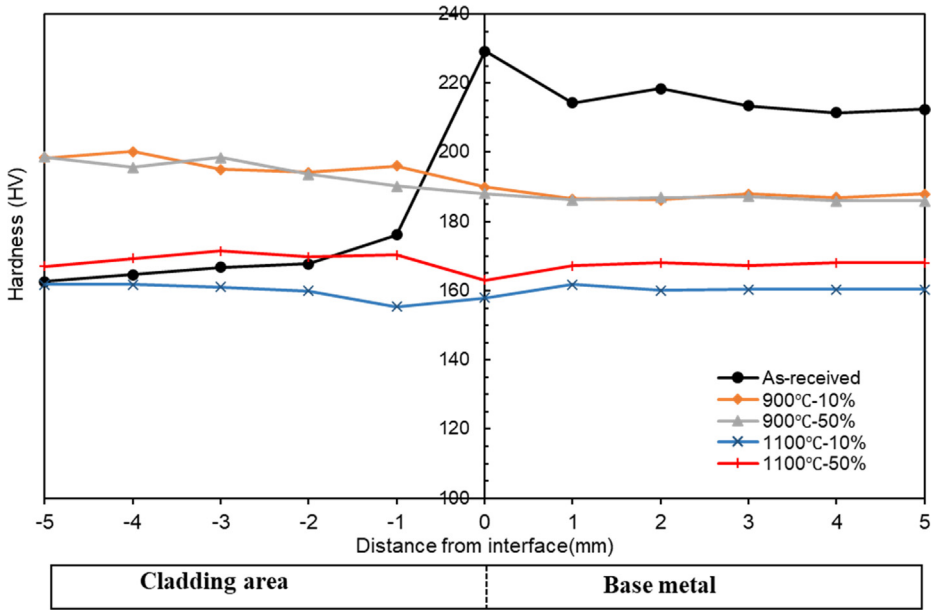

Fig. 12. Vickers microhardness values distribution across the interface layer and the measurement distance was 5 mm away from the interface at 1 mm step size. The hardness values are the mean values of five measurements along the radial direction.

the specimen compressed at 900 °C is higher than that of the specimen compressed at 1100 °C. At 1100 °C, the higher strain level resultes in higher hardness. The hardness of specimen compressed at 1100 °C ~ 0.1 is around 160 HV and the hardness of specimen compressed at 1100 °C ~ 0.5 increases to around 170 HV, close to the hardness of the cladding layer in the as-received specimen.

4. Discussion

4.1. The Gleeble hot compression

The flow stress curves during hot compression are presented in Fig. 2(c). The hardening and softening phenomena could be used to explain the DRV and DRX process. The laser cladding remanufactured samples exhibit different microstructure evolution in the cladding and base parts. During the deformation process to 0.1 engineering strain level, the dislocations were generated and stored in the form of a cellular dislocation arrangement where high dislocation walls enclosed cell interiors of low dislocation density to resistant the deformation [49]. That is consistent with the GNDs density result of Fig. 9(d)-(f), where the highest GNDs density is found at 900 °C ∼ 0.1. This results in the initial hardening behaviour of the hot compression stress–strain curve to a strain level of ∼ 0.1. It also can be explained by the typical Taylor hardening theory [50].

$$\sigma - \sigma_0 = M\alpha b\mu\sqrt{\rho}$$

where σ is flow stress, σ_0 is the flow stress of the material in the absence of dislocation interactions, M is Taylor factor, α is a material constant, b is the burger's vector, and ρ is the dislocation density.

Further deformed to strain level ∼ 0.5 at 900 °C, the DRV and DRX softening occurred as confirmed by Fig. 2(c). These two softening mechanisms lowered the dislocation density and the formed finer grain structure resulted in easier grain boundary sliding and further softening effect. There is no flow stress peak associated with the onset of the DRX process for this material, which is also consistent with previous research in 316L SS [51,52]. It was found that the GND density at the cladding layer was higher than base metal after compression at 900 °C ∼ 0.5. Jiang et al. suggested that grain size and neighbouring grain orientation would influence the GNDs density distribution [53]. As the initial hardness at the cladding layer, interface and base mental is not similar, the flow stress behaviour is not the same. It could be inferred that the softer part of the sample, i.e. the cladding half, is prone to reach the yield point firstly and plastically deformed to higher strain level to the base metal half. Thus, more plasticity and dislocation activities occur at the softer half.

For specimen compressed at the higher deformation temperature (1100 °C), the flow stress is lower than 900 °C, because of the required critical resolved shear stress is lower to initiate the dislocation slip. Grain growth was generally found, as seen in Fig. 4. This resulted in the difficulty in grain boundary sliding, such that gently higher flow stress was seen.

4.2. The hardness variations

The hardness revealed the local mechanical properties across these AM remanufactured samples. This local information can be correlated with the EBSD measured microstructure information at the corresponding areas. For the as-received specimen, the hardness of the base metal is about 215 HV that is higher than the hardness of the cladding layer due to the grain size effect as the dislocation distribution is approximately same. The hardness across the cladding layer increased after hot compression at 900 °C. For the specimen compressed at 900 °C ∼ 0.1, grain size at cladding layer kept constant, but the GNDs density was increased significantly at 900 °C ∼ 0.1 resulting in higher hardness. The specimen compressed at 900 °C ∼ 0.5, significantly reduced grain size and slightly increased GNDs density at the cladding layer than the as-received specimen. This resulted in an increase in hardness. The grain size of the cladding layer of specimen compressed at 1100 °C ∼ 0.1 is larger than as-received one, and GNDs density is approximately the same as an as-received cladding layer. Therefore, the hardness of the as-received cladding layer is higher than the specimen compressed at 1100 ∼ 0.1. For the specimen compressed at 1100 °C ∼ 0.5, the grain size reduced compared to the as-received cladding layer and constant GNDs density resulting in higher hardness values.

For the base metal region, the overall hardness decreased after hot deformation. The dislocation hardening played a more predominant role rather than the grain size. The grain size at the base metal part increased significantly after compression at 900 °C ∼ 0.1, 1100 °C ∼ 0.1, slightly increased at 1100 °C ∼ 0.5 and decreased at 900 °C ∼ 0.5. For the specimen with increasing grain size, the GNDs density for base metal also decreased at 1100 °C ∼ 0.1 and 1100 °C ∼ 0.5. Hence, the hardness for these two conditions was decreased.

Fig. 6 shows that the smaller grain size at the interface comparing to the cladding layer and base metal which did not exhibit the highest hardness. This could be due to the counterbalancing strengthening effect of the medium dislocation density level. Overall, the cladding layer is softer than the base metal for the as-received direct laser cladding remanufacturing part. After the hot compression, the hardness of the laser cladding regions is slightly higher than the base metal. The cladding layer can act as a harder and protective layer to the base metal.

4.3. Temperature and strain effects

The stress–strain behaviour in Fig. 11 shows that the hot compression temperature mainly determines the yield strength. The higher temperature could reduce the yield strength significantly. The ductility, UTS and fracture toughness can be improved by the plastic strain as the DRX is promoted. The UTS and elongation were all increased compared with the as-received specimen when compressed to 0.5 strain level at both temperatures.

However, as the temperature increases, the difference in toughness and ductility of specimen compressed to different strain level become smaller as the DRV was active at the high temperature to consume more dislocations in both cases. In addition, the grain growth caused by grain boundary migration was found at the higher temperature. Therefore, the best fracture toughness was obtained in the specimen compressed at 900 °C ∼ 0.5. Under such condition, effectively grain refinement was achieved.

The proposed hybrid AM and hot compressed samples mechanically behaved competitively to the conventionally wrought ones. This is in good agreement with the previous AMed and hot forging research work [30]. The relatively uniform microhardness distribution of processed specimen was mainly attributed to the recrystallized homogeneous grain and dislocation density structures.

5. Conclusions

To improve the mechanical performance of remanufactured parts, a hybrid laser cladding and subsequently hot compression technique is proposed. A detailed understanding of such process was obtained through the stress–strain behaviour, hardness distribution and the underlying microstructure distribution and evolution. The following conclusions can be drawn:

(1) Heterogenous grain morphology and size through the cladding layer, interface and base metal was shown in the laser cladding specimens. This resulted in a large hardness variation across the interface. This hardness variation can be removed utilizing the hot compression process.

(2) The effect of the hot compression process on the laser clad 316L SS parts was quantitively assessed. The optimal tensile performance was achieved in the sample compressed at 900 °C with a strain level of 0.5. Significantly improvement in mechanical properties was exhibited.
(3) Hot compression at 900 °C hardened the cladding layer significantly, enabling it to act as a protective layer to the base metal.
(4) The yield strength and ductility of the processed samples were determined by compression temperature and strain, which caused the dynamic recrystallization and led to the grain and dislocation density evolution.

CRediT authorship contribution statement

Yuehan Liu: Data curation, Formal analysis, Investigation, Methodology, Writing – original draft, Writing – review & editing. **Yaping Wang:** Formal analysis, Methodology, Writing – review & editing. **Xin Xu:** Formal analysis, Writing – review & editing. **Christopher Hopper:** Formal analysis, Writing – review & editing. **Hongbiao Dong:** Conceptualization, Formal analysis, Writing – review & editing. **Xingtao Wang:** Conceptualization, Formal analysis, Writing – review & editing. **Hongbin Zhu:** Conceptualization, Formal analysis, Writing – review & editing. **Jun Jiang:** Conceptualization, Formal analysis, Supervision, Project administration, Writing – review & editing.

Declaration of Competing Interest

The authors declare that they have no known competing financial interests or personal relationships that could have appeared to influence the work reported in this paper.

Acknowledgements

The authors would like to thank CRRC Industrial Academy Co., Ltd, China for the sample preparation support. X. Xu thanks the support by Innovation Group Project of Southern Marine Science and Engineering Guangdong Laboratory (Zhuhai) (No.311021013). Jun Jiang would like to thank Royal Society International Exchange grant IEC \NSFC\181520.

Data availability

The raw/processed data required to reproduce these findings cannot be shared at this time as the data also forms part of an ongoing study.

References

[1] B. Onuike, A. Bandyopadhyay, Additive manufacturing in repair: Influence of processing parameters on properties of Inconel 718, Mater. Lett. 252 (2019) 256–259, https://doi.org/10.1016/j.matlet.2019.05.114.
[2] A. Saboori, A. Aversa, G. Marchese, S. Biamino, M. Lombardi, P. Fino, Application of directed energy deposition-based additive manufacturing in repair, Appl. Sci. 9 (2019) 3316, https://doi.org/10.3390/app9163316.
[3] J. Yan, M. Gao, X. Zeng, Study on microstructure and mechanical properties of 304 stainless steel joints by TIG, laser and laser-TIG hybrid welding, Opt. Lasers Eng. 48 (4) (2010) 512–517, https://doi.org/10.1016/j.optlaseng.2009.08.009.
[4] S. Nowotny, S. Scharek, E. Beyer, K.-H. Richter, Laser Beam Build-Up Welding: Precision in Repair, Surface Cladding, and Direct 3D Metal Deposition, J. Therm. Spray Technol. 16 (3) (2007) 344–348, https://doi.org/10.1007/s11666-007-9028-5.
[5] W.J. Oh, W.J. Lee, M.S. Kim, J.B. Jeon, D.S. Shim, Repairing additive-manufactured 316L stainless steel using direct energy deposition, Opt. Laser Technol. 117 (2019) 6–17, https://doi.org/10.1016/J.OPTLASTEC.2019.04.012.
[6] J.M. Yellup, Laser cladding using the powder blowing technique, Surf. Coatings Technol. 71 (2) (1995) 121–128, https://doi.org/10.1016/0257-8972(94)01010-G.
[7] W.J. Chen, H. Chen, C.C. Li, X. Wang, Q. Cai, Microstructure and fatigue crack growth of EA4T steel in laser cladding remanufacturing, Eng. Fail. Anal. 79 (2017) 120–129, https://doi.org/10.1016/J.ENGFAILANAL.2017.03.005.
[8] A. Hinojos, J. Mireles, A. Reichardt, P. Frigola, P. Hosemann, L.E. Murr, R.B. Wicker, Joining of Inconel 718 and 316 Stainless Steel using electron beam melting additive manufacturing technology, Mater. Des. 94 (2016) 17–27, https://doi.org/10.1016/j.matdes.2016.01.041.
[9] B. Graf, S. Ammer, A. Gumenyuk, M. Rethmeier, Design of Experiments for Laser Metal Deposition in Maintenance, Repair and Overhaul Applications, Procedia CIRP. 11 (2013) 245–248, https://doi.org/10.1016/J.PROCIR.2013.07.031.
[10] C. Shuai, Y. Cheng, Y. Yang, S. Peng, W. Yang, F. Qi, Laser additive manufacturing of Zn-2Al part for bone repair: Formability, microstructure and properties, J. Alloys Compd. 798 (2019) 606–615, https://doi.org/10.1016/j.jallcom.2019.05.278.
[11] D. Ding, Z. Pan, D. Cuiuri, H. Li, Wire-feed additive manufacturing of metal components: technologies, developments and future interests, Int. J. Adv. Manuf. Technol. 81 (1-4) (2015) 465–481, https://doi.org/10.1007/s00170-015-7077-3.
[12] M. Ma, Z. Wang, X. Zeng, A comparison on metallurgical behaviors of 316L stainless steel by selective laser melting and laser cladding deposition, Mater. Sci. Eng. A. 685 (2017) 265–273, https://doi.org/10.1016/J.MSEA.2016.12.112.
[13] L. Sexton, S. Lavin, G. Byrne, A. Kennedy, Laser cladding of aerospace materials, J. Mater. Process. Technol. 122 (1) (2002) 63–68, https://doi.org/10.1016/S0924-0136(01)01121-9.
[14] J. Leunda, C. Soriano, C. Sanz, V.G. Navas, Laser Cladding of Vanadium-Carbide Tool Steels for Die Repair, in, Phys. Procedia, Elsevier (2011) 345–352, https://doi.org/10.1016/J.PHPRO.2011.03.044.
[15] J. Sampedro, I. Pérez, B. Carcel, J.A. Ramos, V. Amigó, Laser Cladding of TiC for Better Titanium Components, in, Phys. Procedia, Elsevier (2011) 313–322, https://doi.org/10.1016/J.PHPRO.2011.03.040.
[16] S. Sun, Q. Liu, M. Brandt, Microstructure and mechanical properties of laser cladding repair of AISI 4340 steel, Sciences (New. York) 1 (2012) 9.
[17] K.G.F. Janssens, D. Raabe, E. Kozeschnik, M.A. Miodownik, B. Nestler, Computational materials engineering: an introduction to microstructure evolution, Academic Press, 2010.
[18] K.V. Wong, A. Hernandez, A Review of Additive Manufacturing, ISRN Mech. Eng. 2012 (2012) 1–10, https://doi.org/10.5402/2012/208760.
[19] Y. Kok, X.P. Tan, P. Wang, M.L.S. Nai, N.H. Loh, E. Liu, S.B. Tor, Anisotropy and heterogeneity of microstructure and mechanical properties in metal additive manufacturing: A critical review, Mater. Des. 139 (2018) 565–586, https://doi.org/10.1016/j.matdes.2017.11.021.
[20] A. Yadollahi, N. Shamsaei, Additive manufacturing of fatigue resistant materials: Challenges and opportunities, Int. J. Fatigue. 98 (2017) 14–31, https://doi.org/10.1016/j.ijfatigue.2017.01.001.
[21] W.E. King, A.T. Anderson, R.M. Ferencz, N.E. Hodge, C. Kamath, S.A. Khairallah, A.M. Rubenchik, Laser powder bed fusion additive manufacturing of metals; physics, computational, and materials challenges, Appl. Phys. Rev. 2 (4) (2015) 041304, https://doi.org/10.1063/1.4937809.
[22] W.A. Witzen, A.T. Polonsky, T.M. Pollock, I.J. Beyerlein, Three-dimensional maps of geometrically necessary dislocation densities in additively manufactured Ni-based superalloy IN718, Int. J. Plast. 131 (2020) 102709, https://doi.org/10.1016/j.ijplas.2020.102709.
[23] M. Gäumann, S. Henry, F. Cléton, J.-D. Wagnière, W. Kurz, Epitaxial laser metal forming: analysis of microstructure formation, Mater. Sci. Eng. A. 271 (1999) 232–241, https://doi.org/10.1016/S0921-5093(99)00202-6.
[24] R.W. Armstrong, 60 Years of Hall-Petch: Past to Present Nano-Scale Connections, Mater. Trans. 55 (1) (2014) 2–12, https://doi.org/10.2320/matertrans.MA201302.
[25] K. Zhang, S. Wang, W. Liu, X. Shang, Characterization of stainless steel parts by Laser Metal Deposition Shaping, Mater. Des. 55 (2014) 104–119, https://doi.org/10.1016/j.matdes.2013.09.006.
[26] M. Godec, S. Zaefferer, B. Podgornik, M. Šinko, E. Tchernychova, Quantitative multiscale correlative microstructure analysis of additive manufacturing of stainless steel 316L processed by selective laser melting, Mater. Charact. 160 (2020), https://doi.org/10.1016/j.matchar.2019.110074 110074.
[27] H. Paydas, A. Mertens, R. Carrus, J. Lecomte-Beckers, Tchoufang Tchuindjang, Laser cladding as repair technology for Ti-6Al-4V alloy: Influence of building strategy on microstructure and hardness, Mater. Des. 85 (2015) 497–510, https://doi.org/10.1016/j.matdes.2015.07.035.
[28] J. Jiang, P. Hooper, N. Li, Q. Luan, C. Hopper, M. Ganapathy, J. Lin, An integrated method for net-shape manufacturing components combining 3D additive manufacturing and compressive forming processes, Procedia Eng., Elsevier Ltd (2017) 1182–1187, https://doi.org/10.1016/j.proeng.2017.10.1050.
[29] C.I. Pruncu, C. Hopper, P.A. Hooper, Z. Tan, H. Zhu, J. Lin, J. Jiang, Study of the Effects of Hot Forging on the Additively Manufactured Stainless Steel Preforms, J. Manuf. Process. 57 (2020) 668–676, https://doi.org/10.1016/j.jmapro.2020.07.028.
[30] B. Weiss, R. Stickler, Phase instabilities during high temperature exposure of 316 austenitic stainless steel, Met Trans. 3 (4) (1972) 851–866, https://doi.org/10.1007/BF02647659.
[31] C. Wang, T.G. Liu, P. Zhu, Y.H. Lu, T. Shoji, Study on microstructure and tensile properties of 316L stainless steel fabricated by CMT wire and arc additive manufacturing, Mater. Sci. Eng. A. 796 (2020) 140006, https://doi.org/10.1016/j.msea.2020.140006.

[32] M. Godec, S. Zaefferer, B. Podgornik, M. Šinko, E. Tchernychova, Quantitative multiscale correlative microstructure analysis of additive manufacturing of stainless steel 316L processed by selective laser melting, Mater. Charact. 160 (2020) 110074, https://doi.org/10.1016/j.matchar.2019.110074.
[33] R.I. Revilla, M. Van Calster, M. Raes, G. Arroud, F. Andreatta, L. Pyl, P. Guillaume, I. De Graeve, Microstructure and corrosion behavior of 316L stainless steel prepared using different additive manufacturing methods: A comparative study bringing insights into the impact of microstructure on their passivity, Corros. Sci. 176 (2020) 108914, https://doi.org/10.1016/j.corsci.2020.108914.
[34] L. Wang, J. Xue, Q. Wang, Correlation between arc mode, microstructure, and mechanical properties during wire arc additive manufacturing of 316L stainless steel, Mater. Sci. Eng. A. 751 (2019) 183–190, https://doi.org/10.1016/J.MSEA.2019.02.078.
[35] S. Venugopal, M. Vasudevan, Sridhar Venugopal, P.V. Sivaprasad, S.K. Jha, P. Pandey, S.L. Mannan, Y.V.R.K. Prasad, Industrial validation of processing maps of 316L stainless steel using hot forging, rolling, and extrusion, Mater. Sci. Technol. 12 (11) (1996) 955–962, https://doi.org/10.1179/mst.1996.12.11.955.
[36] W. Pantleon, Resolving the geometrically necessary dislocation content by conventional electron backscattering diffraction, Scr. Mater. 58 (11) (2008) 994–997, https://doi.org/10.1016/j.scriptamat.2008.01.050.
[37] A.H. Maamoun, M. Elbestawi, G.K. Dosbaeva, S.C. Veldhuis, Thermal post-processing of AlSi10Mg parts produced by Selective Laser Melting using recycled powder, Addit. Manuf. 21 (2018) 234–247, https://doi.org/10.1016/j.addma.2018.03.014.
[38] Linkan Bian, Scott M. Thompson, Nima Shamsaei, Mechanical properties and microstructural features of direct laser-deposited Ti-6Al-4V, Jom. 67 (3) (2015) 629–638, https://doi.org/10.1007/s11837-015-1308-9.
[39] B.E. Carroll, T.A. Palmer, A.M. Beese, Anisotropic tensile behavior of Ti-6Al-4V components fabricated with directed energy deposition additive manufacturing, Acta Mater. 87 (2015) 309–320, https://doi.org/10.1016/j.actamat.2014.12.054.
[40] L. Chechik, N.A. Boone, L.R. Stanger, P. Honniball, F. Freeman, G. Baxter, J.R. Willmott, I. Todd, Variation of texture anisotropy and hardness with build parameters and wall height in directed-energy-deposited 316L steel, Addit. Manuf. 38 (2021), https://doi.org/10.1016/j.addma.2020.101806 101806.
[41] A. Hadadzadeh, F. Mokdad, M.A. Wells, D.L. Chen, A new grain orientation spread approach to analyze the dynamic recrystallization behavior of a cast-homogenized Mg-Zn-Zr alloy using electron backscattered diffraction, Mater. Sci. Eng. A. 709 (2018) 285–289, https://doi.org/10.1016/j.msea.2017.10.062.
[42] J. Jiang, T.B. Britton, A.J. Wilkinson, Evolution of dislocation density distributions in copper during tensile deformation, Acta Mater. 61 (2013) 7227–7239, https://doi.org/10.1016/j.actamat.2013.08.027.
[43] Q. Luan, H. Xing, J. Zhang, J. Jiang, Experimental and crystal plasticity study on deformation bands in single crystal and multi-crystal pure aluminium, Acta Mater. 183 (2020) 78–92, https://doi.org/10.1016/j.actamat.2019.11.006.
[44] J.F. Nye, Some geometrical relations in dislocated crystals, Acta Metall. 1 (2) (1953) 153–162.
[45] M.F. Ashby, The deformation of plastically non-homogeneous materials, Philos. Mag. A J. Theor. Exp. Appl. Phys. 21 (1970) 399–424.
[46] X.Z. Liang, M.F. Dodge, J. Jiang, H.B. Dong, Using transmission Kikuchi diffraction in a scanning electron microscope to quantify geometrically necessary dislocation density at the nanoscale, Ultramicroscopy 197 (2019) 39–45, https://doi.org/10.1016/j.ultramic.2018.11.011.
[47] M. Shamsujjoha, S.R. Agnew, J.M. Fitz-Gerald, W.R. Moore, T.A. Newman, High Strength and Ductility of Additively Manufactured 316L Stainless Steel Explained, Metall. Mater. Trans. A. 49 (7) (2018) 3011–3027, https://doi.org/10.1007/s11661-018-4607-2.
[48] A. Yadollahi, N. Shamsaei, S.M. Thompson, D.W. Seely, Effects of process time interval and heat treatment on the mechanical and microstructural properties of direct laser deposited 316L stainless steel, Mater. Sci. Eng. A. 644 (2015) 171–183, https://doi.org/10.1016/j.msea.2015.07.056.
[49] F. Roters, D. Raabe, G. Gottstein, Work hardening in heterogeneous alloys—a microstructural approach based on three internal state variables, Acta Mater. 48 (17) (2000) 4181–4189.
[50] G. Horváth, N.Q. Chinh, J. Gubicza, J. Lendvai, Plastic instabilities and dislocation densities during plastic deformation in Al–Mg alloys, Mater. Sci. Eng. A. 445-446 (2007) 186–192.
[51] L. Chen, R. Luo, Y. Yang, C. Peng, X. Gui, J. Zhang, K. Song, P. Gao, X. Cheng, Investigation on the Hot Deformation Behavior of 316L Stainless Steel Using 3D Processing Map, Trans. Indian Inst. Met. 72 (12) (2019) 2997–3006.
[52] S.-H. Song, A Comparison Study of Constitutive Equation, Neural Networks, and Support Vector Regression for Modeling Hot Deformation of 316L Stainless Steel, Materials (Basel). 13 (2020) 3766.
[53] J. Jiang, T. Ben Britton, A.J. Wilkinson, The orientation and strain dependence of dislocation structure evolution in monotonically deformed polycrystalline copper, Int. J. Plast. 69 (2015) 102–117, https://doi.org/10.1016/j.ijplas.2015.02.005.